Decay times of atmospheric acoustic-gravity waves after deactivation of wave forcing

Nikolai M. Gavrilov[1], Sergey P. Kshevetskii[1,2], Andrey V. Koval[1,3]

[1]Atmospheric Physics Department, Saint-Petersburg State University, Saint Petersburg, 199034, Russia
5 [2]Physics Department, Immanuel Kant Baltic Federal University, Kaliningrad, 236016, Russia
[3]Meteorological Forecast Department, Russian State Hydro-meteorological University, Saint Petersburg, 192007, Russia

Correspondence to: Nikolai M. Gavrilov (n.gavrilov@spbu.ru)

Abstract. High-resolution numerical simulations of non-stationary nonlinear acoustic-gravity waves (AGWs) propagating
10 upwards from surface wave sources are performed for different temporal intervals relative to activation/deactivation times of
the wave forcing. After activating surface wave sources, amplitudes of AGW spectral components reach a quasi-stationary
state. Then the surface wave forcing is deactivated in the numerical model, and amplitudes of vertically traveling AGW
modes quickly decrease at all altitudes due to discontinuations of the upward propagation of wave energy from the wave
sources. However, later the standard deviation of residual and secondary wave perturbations experiences slower quasi-
15 exponential decrease. High-resolution simulations allowed, for the first time, estimating the decay times of this wave noise
produced by slow residual, quasi-standing and secondary AGW spectral components, which vary between 20 and 100 hrs
depending on altitude and the rate of wave source activation/deactivation. The standard deviations of the wave noise are
larger for the case of sharp activation/deactivation of the wave forcing compared to the steep processes. These results show
that transient wave sources may create long-lived wave perturbations, which can form a background level of wave noise in
20 the atmosphere. This should be taken into account in parameterizations of atmospheric AGW impacts.

1 Introduction

Recently, acoustic-gravity waves (AGWs) are believed to exist almost permanently in the atmosphere (e.g., Fritts and
Alexander, 2003). Observations detect regular AGW presence up to high atmospheric altitudes (e.g., Djuth et al., 2004; Park
et al., 2014). Modeling of general circulation demonstrated AGWs capabilities of transferring energy and momentum from
25 tropospheric wave sources to higher atmospheric levels (e.g., Medvedev and Yiğit, 2019). Non-hydrostatic models of the
general circulation of the atmosphere revealed that AGWs are permanently existed at all atmospheric heights (e.g. Yiğit et
al., 2012b).

Many AGWs detected in the atmosphere are excited in the troposphere (Fritts and Alexander, 2003; Yiğit et al., 2014).
AGWs can be produced by interactions of winds with mountains (e.g., Gossard and Hook, 1975), atmospheric jet streams
30 and fronts (e.g., Gavrilov and Fukao, 1999; Dalin et al., 2016), thunderstorms and cumulus clouds (Blanc et al., 2014),

convective regions and shear flows (Townsend, 1966; Fritts and Alexander , 2003; Vadas and Fritts, 2006), typhoons (Wu et al.,2015), volcanoes (De Angelis et al., 2011), waves on the sea surface (Godin et al., 2015), by explosions at the Earth's surface (Meng, 2019), earthquakes (Rapoport et al., 2004), different objects moving in the atmosphere (Afraimovich et al., 2002), big fires, etc. Some AGWs can be generated by mesoscale turbulence in the atmosphere (Townsend, 1965; Medvedev

35 and Gavrilov, 1995). These AGW sources are located mainly at tropospheric heights (Gavrilov and Fukao, 1999; Dalin, 1916).

Most wave sources listed above are non-stationary. They can be activated during initial time intervals, operate for some time, and then can be deactivated during final time intervals. The initial and final time intervals could be shorter or longer depending on the physical properties of particular wave sources. Non-stationary activating and deactivating wave sources

40 can generate transient AGW pulses propagating upwards from the lower atmosphere, which require there analysis.

High-resolution numerical models are frequently used for studies of meso- and microscale processes in the atmosphere. For example, the Weather Research and Forecasting Non-hydrostatic Mesoscale Model known also as the North American Mesoscale model (WRF, 2019), as well as the Regional Atmospheric Modeling System (RAMS) described by Pielke et al. (1992) and other similar models. Direct Numerical Simulation (DNS) and Large Eddy Simulation (LES) models (e.g.,

45 Mellado, 2018) should be mentioned in this context. Fritts et al. (2009, 2011) used a numerical model of Kelvin-Helmholtz instabilities, AGW breaking and generation of turbulence in atmospheric regions with fixed horizontal and vertical extents. They utilized a Galerkin-type algorithm for turning partial differential equations into equations for spectral series coefficients. Liu et al. (2009) simulated propagations of atmospheric AGWs and creation of Kelvin-Helmholtz billows. Yu et al. (2017) used a numerical model for AGWs propagating in the atmosphere from tsunamis.

50 Gavrilov and Kshevetskii (2013) studied nonlinear AGWs with a numerical two-dimensional model, which involved fundamental conservation laws. This model permitted non-smooth solutions of the nonlinear wave equations and gave the required stability of the numerical model (Kshevetskii and Gavrilov, 2005). A respective three-dimensional algorithm was introduced by Gavrilov and Kshevetskii (2014) to simulate nonlinear atmospheric AGWs. Gavrilov and Kshevetskii (2013. 2014) showed that after triggering wave forcing at the lower boundary of numerical model, initial AGW pulses could reach

55 high atmospheric levels in a few minutes. AGW phase surfaces are quasi-vertical initially, but later they become inclined to the horizon. AGW vertical wavelengths decrease in time and are close to their theoretical predictions after intervals of a few periods of wave forcing.

In this study, using the high-resolution nonlinear wave model developed by Gavrilov and Kshevetskii (2014), we continue simulating transient waves generated by non-stationary AGW sources at the lower boundary and propagating

60 upwards to the atmosphere. The main focus is AGW behavior after deactivations of wave sources in the model. After activating the surface wave source and disappearing initial wave pulses, AGW amplitudes tend to stabilize at all atmospheric altitudes. In this quasi-stationary state, the surface wave forcing is deactivated in the numerical model. After that, amplitudes of traveling AGW modes quickly decrease at all altitudes due to discontinuation of the upward propagation of wave energy

from the surface sources. We found, however, that after some time, the standard deviation of residual quasi-standing and
65 secondary wave perturbations experiences more slow exponential decrease with substantial decay times.

These results show that residual and secondary AGW modes produced by transient wave sources can exist for long time
in the stratosphere and mesosphere and form a background level of wave noise there. AGW decay times and their
dependences on parameters of the surface wave forcing are estimated for the first time.

2 Numerical model

70 In this study, we employed the high-resolution three-dimentional numerical model of nonlinear AGWs in the atmosphere
developed by Gavrilov and Kshevetskii (2014). Currently, this model (called as AtmoSym) is available for free online usage
(AtmoSym, 2017). The AtmoSym model utilizes the plain geometry and primitive hydrodynamic three-dimensional
equations (Gavrilov and Kshevetskii, 2014):

$$\frac{\partial \rho}{\partial t} + \frac{\partial \rho v_\beta}{\partial x_\beta} = 0, \;\; \rho c_p \frac{dT}{dt} = \frac{dp}{dt} + \rho\varepsilon, \;\; p = \rho RT,$$

75
$$\frac{\partial \rho v_i}{\partial t} + \frac{\partial \rho v_i v_\beta}{\partial x_\beta} = -\frac{\partial p}{\partial x_i} - \rho g \delta_{i3} + \frac{\partial \sigma_{i\beta}}{\partial x_\beta}, \;\; i, \beta = 1, 2, 3, \tag{1}$$

where t is time; p, ρ, T are pressure, density and temperature, respectively; v_β are velocity components along the coordinate
axes x_β; $\sigma_{i\beta}$ is the viscous stress tensor; g is the acceleration due to gravity; c_p is the specific heat capacity at constant
pressure; R is the atmospheric gas constant; ε is the specific heating rate; $d/dt = \partial/\partial t + v_\beta \partial/\partial x_\beta$; repeating Greek indexes
assume summation. Quantities $\sigma_{i\beta}$ and ε in Eq. (1) contain stresses and heating rates produced by molecular viscosity and
80 heat conductivity (see details in Gavrilov and Kshevetskii, 2014). After numerical integration of Eq. (1), dynamical
deviations (marked with primes below) from stationary background values p_0, ρ_0, T_0 and v_{i0} are calculated:

$$p' = p - p_0; \;\; \rho' = \rho - \rho_0; \;\; T' = T - T_0; \;\; v'_i = v_i - v_{i0}. \tag{2}$$

The AtmoSym model takes into account dissipative and nonlinear processes accompanied AGW propagation. The model is
capable to simulate such complicated processes as AGW instability, breaking and turbulence generation. Dynamical
85 deviations (2) describe both wave perturbations and modifications of background fields due to momentum and energy
exchange between dissipating AGWs and the atmosphere. The background temperature $T_0(z)$ is obtained from the semi-
empirical NRLMSISE-00 atmospheric model (Picone et al., 2001). Background dynamic molecular viscosity, μ_0, and heat
conductivity, κ_0, are estimated using the Sutherland's formulae (Kikoin, 1976):

$$\mu_0 = \frac{1.46 \times 10^{-6} \sqrt{T_0}}{1 + 110/T_0} \quad \left(\frac{kg}{m \cdot s}\right)$$

$$\kappa_0 = \frac{\mu_0}{\mathrm{Pr}}; \quad \mathrm{Pr} = \frac{4\gamma}{9\gamma - 5}, \tag{3}$$

90   where γ is the heat capacity ratio, Pr is the Prandtl number. The AtmoSym model involves also the mean turbulent thermal conductivity and viscosity having maxima about 10 m^2s^{-1} in the boundary layer and in the lower thermosphere, and a broad minimum up to 0.1 m^2s^{-1} in the stratosphere (Gavrilov and Kshevetskii, 2014). The upper boundary conditions at $z = h$ have the following form (Kurdyaeva et al., 2018):

$$\left(\frac{\partial T}{\partial z}\right)_{z=h} = 0, \quad \left(\frac{\partial v_1}{\partial z}\right)_{z=h} = 0, \quad \left(\frac{\partial v_2}{\partial z}\right)_{z=h} = 0, \quad \left(w\right)_{z=h} = 0, \quad (4)$$

95   where indices 1 and 2 correspond to horizontal directions, $w = v_3$ is vertical velocity. Conditions (4) may cause reflections of AGWs coming from below. The upper boundary at the present study is set at $h = 600$ km, where molecular viscosity and heat conductivity are very high and reflected waves are strongly dissipated. Sensitivity tests reveal that the impact of conditions at the upper boundary (4) is negligible at altitudes $z < h - 2H$, where H is the atmospheric scale height. Therefore, at altitudes of the middle atmosphere analyzed in this paper, the influence of the upper boundary conditions (4) could be

100   negligible. The lower boundary conditions at the Earth's surface have the following form (see Kurdyaeva et al., 2018):

$$\left(T'\right)_{z=0} = 0, \quad \left(v_1\right)_{z=0} = 0, \quad \left(v_2\right)_{z=0} = 0, \quad \left(w\right)_{z=0} = W_0 \cos(\sigma t - \vec{k} \cdot \vec{r}), \quad (5)$$

where W_0 and σ have sense of the amplitude and frequency, $\vec{k} = (k_1, k_2)$ is the horizontal wave vector, $\vec{r} = (x_1, x_2)$ is the position vector in the horizontal plane, k_1 and k_2 are the wavenumbers along horizontal axes x_1 and x_2, respectively. The last relation for the surface vertical velocity in (5) serves as the source of plane AGW modes in the AtmoSym model. Such plane

105   modes can represent spectral components of tropospheric dynamical processes. Their effects can be approximated by appropriate sets of effective spectral components of vertical velocity at the lower boundary (Townsend, 1965, 1966). Along horizontal axes x_1 and x_2, one can assume periodicity of wave fields

$$F(x_1, x_2, z, t) = F(x_1 + L_1, x_2 + L_2, z, t), \quad (6)$$

where F denotes any of simulated hydrodynamic quantities, $L_1 = n_1\lambda_1$ and $L_2 = n_2\lambda_2$ are horizontal dimensions of the

110   analyzed atmospheric region; $\lambda_1 = 2\pi/k_1$ и $\lambda_2 = 2\pi/k_2$ are wavelengths along axes x_1 and x_2, respectively; n_1 and n_2 are integers.

In our simulations, the wave excitation (5) is activated at the moment $t = t_a$ and then its amplitude W_0 does not change for some time. One should expect that at small amplitudes of wave source (5), the numerical solutions in the lower and middle atmosphere should tend at $t \gg t_a$ to a steady-state plane AGW modes corresponding to the traditional linear theory (e.g.,

115   Gossard and Hooke, 1975). Gavrilov and Kshevetskii (2015) showed good agreement of ratios of simulated amplitudes of different wave fields with polarization relations of linear AGW theory (Gossard and Hooke, 1975) at $t \gg t_a$ at altitudes up to 100 km.

The novelty of the present study is deactivating the wave source (5) at some moment $t = t_d$ after reaching the described

above quasi-steady solution. Previous simulations with the AtmoSym model showed that sharp activating surface wave

120   source (5) could create an initial AGW pulse, which can reach high altitudes in a few minutes. To control the rate of the

wave source activation/deactivation, in the present simulations, we multiply the surface vertical velocity in (5) by a function

$$q(t) = \begin{cases} \exp[-(t-t_a)^2 / s_a^2] & at & t \le t_a \\ 1 & at & t_a < t < t_d \\ \exp[-(t-t_d)^2 / s_d^2] & at & t \ge t_d \end{cases} \qquad (7)$$

where s_a and s_d are constants.

3 Results of numerical simulations

125   Our numerical modeling begins from steady state windless non-perturbed atmosphere with profiles of background

temperature, density, molecular weight and molecular kinematic viscosity corresponding to January at latitude 50° N at

medium solar activity according to the NRLMSISE00 model (Picone et al., 2001), which are presented in Figure 1 of the

paper by Gavrilov et al. (2018).

   In this study, we consider AGW modes propagating along the eastward axis x and use horizontal dimension of considered

130   atmospheric region to be equal to the circle of latitude at 50°N, which is $L_x \approx$ 27000 km. At horizontal boundaries of this

circle of latitude, we use periodical boundary conditions (6). Representing the circle of latitude by a rectangle area assumes

fixed L_x at all altitudes, while in spherical coordinates L_x is increasing in altitude. However, the differences in L_x at altitudes

of the middle atmosphere do not exceed 2%. Modeling was performed with the surface wave source (5) for AGW modes

having amplitudes $W_0 = 0.01 – 0.1$ mm/s and horizontal phase speeds $c_x \sim$ 50 - 200 m/s. The number of wave periods along

135   the circle of latitude is taken to be $n_1 = 32$. This corresponds the horizontal wavelength $\lambda_x = L_x/n_1 \approx$ 844 km and AGW

periods $\tau = \lambda_x/c_x \sim 4.7 – 1.2$ hr for the specified above range of c_x values. The horizontal grid spacing of the numerical model

is $\Delta x = \lambda_x/16$ and the time step of calculations was automatically adjusted to $\Delta t \approx 2.9$ s. The vertical grid of the model covers

altitudes up to $h = 600$ km and contains 1024 non-equidistant nodes. Vertical spacing varies between 12 m and 3 km from the

lower to the upper boundary, so about 70% grid nodes are located in the lower and middle atmosphere.

140   For parameters of the smoothing factor (7) in the present simulations, we take $t_a = 10^5$ s ≈ 28 hr and $t_d = 4 \times 10^5$ s ≈ 110 hr,

and consider steep AGW source activating and deactivating with $s_a = s_d = 3.3 \times 10^4$ s ≈ 9 hr and sharp triggering at $s_a = s_d =$

0.3 s. The shape of smoothing factor (7) influences the spectrum of the surface wave source in the model. Figure 1 shows

spectra of the sinusoidal source (5) with wave period $\tau = 2\pi/ \sigma = 2$ hr, which were calculated using 20-hour running time

intervals corresponding to the phases of activation, activated state and deactivation of the wave source (5) with the

145   mentioned above "steep" and "sharp" values of s_a and s_d in Eq. (7). Comparisons of solid and dashed lines in Figure 1 show

that the sharp activation and deactivation of the wave source decreases the spectral density at frequency of the main spectral

maximum. However, the sharp triggering considerably increases the high-frequency part of the wave spectra in Figure 1, which means larger proportions of acoustic waves generated by quickly varying wave sources in the atmosphere.
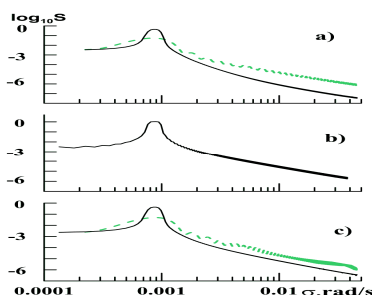
150 **Figure 1.** Spectral density (in relative units) of the surface wave source (5) having period of 2 hr for 20-hour running time intervals centered at model times $t \approx 20$ hr (a), $t \approx 70$ hr (b) and $t \approx 120$ hr (c), which correspond to the wave forcing activation, activated state and deactivation. Solid and dashed lines correspond to the steep and sharp activation/deactivation rates s_a and s_d in (7).

3.1 Steep wave source triggering

155 Figure 2 shows time variations of the standard deviation of wave vertical velocity δw at different altitudes averaged over one horizontal wavelength for the steep activation and deactivation of the surface wave source (5) with $W_0 = 0.01$ mm/s and $c_x = 50$ m/s. The standard deviation δw is proportional to the amplitude of wave variations of vertical velocity. Vertical dashed lines in Figure 2 show moments $t = t_a \approx 28$ hr and $t = t_d \approx 110$ hr of the surface wave source activation and deactivation in (7). The bottom left panel of Figure 2 for the Earth's surface shows that the wave source amplitude increases steeply at $t < t_a$, 160 maintains constant at $t_a < t < t_d$ and steeply decreases to zero at $t > t_d$ in accordance with (7).
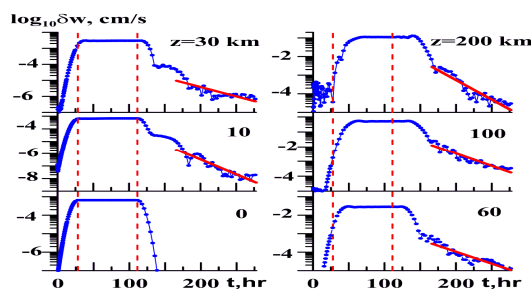
Figure 2. Time variations of standard deviations of the wave vertical velocity at different altitudes (marked with numbers) for the steep activation and deactivation of the surface wave source (5) at $c_x = 50$ m/s and $W_0 = 0.01$ mm/s. Dashed lines 165 correspond to $t = t_a$ and $t = t_d$ in (7). Solid lines show exponential fits.

Similar increases in δw during the activation interval $t < t_a$ one can see at all altitudes in Figure 2. At altitudes higher than 60 km noisy components are noticeable in Figure 2 at $t < t_a$, which can be produced by acoustic components of the wave source spectrum shown in Figure 1a. However for the steep smoothing factor $q(t)$ in (7) this acoustic noise is substantially smaller than the wave amplitudes at $t > t_a$ at all altitudes. In Figure 2, one can see later transition to a quasi-stationary wave regime with steady amplitudes at higher altitudes compared to that at the Earth's surface. This reflects a time delay $\tau_e \sim z/c_z$ required for the main modes of internal gravity waves (IGWs) to propagate from the surface to altitude z with the mean vertical group velocity $c_z \sim \lambda_z/\tau$, where λ_z and τ are the mean vertical wavelength and wave period, respectively. For the shown in Figure 2 wave excitation (5) with $\lambda_x = 844$ km and $c_x = 50$ m/s, using the traditional theory of AGWs (e.g., Gossard and Hook, 1975), one can estimate $\tau \sim 4.7$ hr, $\lambda_z \sim 15$ km and $t_e \sim (6.7 - 13.3)\tau \sim 31$ - 62 hr for $z = 100 - 200$ km. This corresponds to the time delays between the moments t_a and achieving quasi-stationary amplitudes at different altitudes in Figure 2.

The main goal of this study is the analysis of wave fields after deactivating of the surface wave source (5), which was made applying (7) with $t_d \approx 110$ hr and $s_d \approx 9$ hr for the steep triggering shown in Figure 2. One can see that after the wave source deactivation, AGW amplitudes start to decrease from their quasi-stationary values at all altitudes with time delays t_e discussed above. Just after the wave forcing deactivating, δw decreases relatively fast similarly to the decrease in the wave source amplitude in the bottom left panel of Figure 2. This may reflect disappearing of fast traveling AGW modes due to discontinuities of their generation after the wave forcing deactivation. However, later, at $t > 170$ hr all panels in Figure 2 demonstrate slower δw decreases, which can be approximated by exponential curves $\delta w \sim exp(-t/\tau_0)$ with the decay times τ_0 presented in Table 1 for different altitudes.

Table 1. AGW decay times τ_0 in hr in the interval $t \sim 170 - 290$ hr at different altitudes for various parameters of the surface wave sources (5) and their time dependences (7).

s_a , s_d	$3 \cdot 10^{-1}$				$3 \cdot 10^4$			
W_0,mm/s	0.01		0.1		0.01		0.1	
C_x, m/s	50	100	50	100	50	100	50	100
z = 10 km	44	47	54	64	17	54	17	53
z= 30 km	67	44	69	46	37	57	34	55
z= 60 km	85	85	69	72	33	98	35	92
z=100 km	53	63	52	72	26	60	24	57
z=200 km	54	41	41	40	21	41	61	54

For the steep deactivation of the low-amplitude wave source shown in Figure 2, the decay times in Table 1 are $\tau_0 \sim 17 - 98$ hr depending on altitude, which is much larger than the time scale of the steep deactivation $s_d \approx 9$ hr. Such slow decay rates may be caused by partial reflections of the wave energy making vertically quasi-standing AGW modes (see section 4).

Contributions may also occur from slow components of wave source spectrum (see Figure 1), which can dominate after the recession of faster primary spectral modes. In addition, slow shortwave AGW modes can be generated by nonlinear wave interactions at all stages of high-resolution simulations. Mentioned quasi-standing, residual and secondary wave modes can

195   slowly travel to higher atmospheric levels and dissipate there due to increased molecular and turbulent viscosity and heat conductivity, which are small in the lower and middle atmosphere. Therefore, decaying these residual and secondary AGW modes may require substantial time intervals after deactivating wave forcing, as one can see in Figure 2.

3.2 Sharp wave source triggering

Figure 3 shows the same standard deviation of wave vertical velocity δw as Figure 2, but for the sharp activation of the

200   surface wave source (5) with $W_0 = 0.01$ mm/s, $c_x = 50$ m/s and parameters in the time factor (7) $t_a \approx 28$ hr, $t_d \approx 110$ hr and $s_a = s_d = 0.3$ s. The initial AGW pulses are more intensive and contain wider ranges of spectral components (see Figures 1a and 1c) in the case of sharp wave source activations/deactivations. The right top panel of Figure 3 shows that at high altitudes the initial wave pulses might be so high that AGW amplitudes do not reach steady-state conditions existing in the respective panel of Figure 2.

205
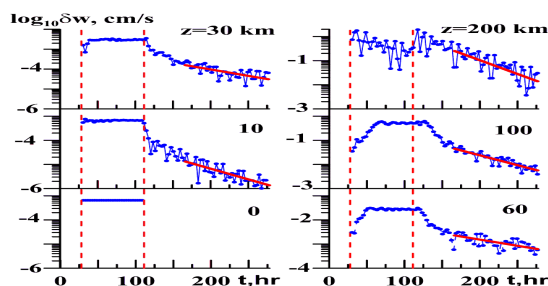
Figure 3. Same as Figure 2, but for the sharp wave source activation.

The right top panel of Figure 3 shows substantial AGW pulses not only at the wave source activation t_a, but also at the

210   moment of wave source sharp deactivation t_d, when δw values have additional maxima at high altitudes. Stronger AGW pulses caused by the sharp wave source activation/deactivation increase proportions of slow quasi-standing, residual and secondary wave components after turning off the wave forcing in the AtmoSym model. Therefore exponential decays of δw start earlier and are more pronounced in Figure 3 than those in the respective panels of Figure 2. AGW decay times τ_0 corresponding to the exponential approximations in Figure 3 for the sharp wave source activation are given in the left

215   column of Table 1 and vary between 44 and 85 days. They are generally larger than the discussed above values of τ_0 in Figure 2, which means that stronger residual wave noise at the sharp wave source triggering require longer time intervals for their decay.

Figures 2 and 3 represents results for the wave source (5) with $c_x = 50$ m/s. Table 1 contains also the decay times for the wave excitation with $c_x = 100$ m/s. Respective primary AGWs have larger vertical wavelengths and should experience

220 smaller molecular and turbulent dissipation in the atmosphere. For the steep activation/deactivation of the wave source (5) with small amplitude $W_0 = 0.01$ mm/s, Table 1 reveals larger values of τ_0 for AGWs with $c_x = 100$ m/s compared to those with $c_x = 50$ m/s. Therefore, smaller dissipation of the faster AGW modes corresponds to longer time for their decay, especially at altitudes below 100 km. For the sharp activation/deactivation of the wave source at $W_0 = 0.01$ mm/s, the left columns of Table 1 shows approximately equal τ_0 values for waves with $c_x = 50$ m/s and $c_x = 100$ m/s.

225 Relative contributions of residual and secondary AGWs can be estimated by the ratio $\delta w/W_0$ at the beginning of the exponential tails in Figures 2 and 3 at $t = 170$ hr, which is presented in Table 2. For the steep wave source activation/deactivation at $s_a = s_d \approx 9$ hr in (7) and $W_0 = 0.01$ mm/s in (5), Table 2 shows smaller ratios of the residual wave noise at altitudes below 200 km for the wave forcing with $c_x = 100$ m/s compared to $c_x = 50$ m/s. At the sharp wave source activation/deactivation at $s_a = s_d \approx 0.3$ s in (7), the ratios of residual waves are larger at all altitudes compared to the steep

230 case in Table 2. For the wave forcing (5) with $c_x = 100$ m/s, the ratios are comparable or smaller at altitudes below 150 km and larger above 150 km compared to the case of $c_x = 50$ m/s. Larger ratios of residual and secondary waves at sharp wave source triggering in Table 2 may explain generally larger AGW decay times τ_0 in the left columns of Table 1 for $W_0 = 0.01$ mm/s, as far as the dissipation of stronger wave noise may require longer time intervals.

235 **Table 2.** Ratios $\delta w(z)/W_0$ at $t = 170$ hr at different altitudes for various parameters of the surface wave source (5) and its time dependence (7).

S_a, s	$3 \cdot 10^{-1}$				$3 \cdot 10^{4}$			
W_0, mm/s	0.01		0.1		0.01		0.1	
c_x, m/s	50	100	50	100	50	100	50	100
z = 10 km	0.015	0.016	0.013	0.013	0.003	0.001	0.003	0.001
z = 30 km	0.158	0.163	0.182	0.190	0.009	0.001	0.011	0.001
z = 60 km	2.272	1.032	2.257	1.147	0.289	0.004	0.257	0.005
z = 100 km	44.58	12.88	42.36	11.97	12.39	0.086	10.55	0.082
z = 200 km	198.3	335.8	277.5	344.7	2.732	0.925	0.426	0.406

3.3 Larger amplitude wave sources

Described above simulations were made for small-amplitude wave sources (5) with $W_0 = 0.01$ mm/s. For larger $W_0 = 0.1$ mm/s, Figure 4 reveals time variations of the vertical velocity standard deviations δw at different altitudes for $c_x = 100$ m/s at

240 the steep wave source activation/deactivation with $s_a = s_d \approx 9$ hr s in (7), which is similar to Figure 2. Below altitude of 100 km, one can see the intervals of quasi-constant AGW amplitudes after the end of the wave source activation at $t = t_a$ (vertical dashed lines in Figure 4). Theoretical time delay t_e between the wave source activation and the beginning of the steady-state

AGW regime is 4 times smaller for $c_x = 100$ km than that for $c_x = 50$ km, as one can see comparing Figures 2 and 4. After deactivations of the surface wave source (5) at $t = t_d$, values of δw in Figure 4 are first decreasing relatively fast due to the

245 discontinuing generation of primary AGW modes at the lower boundary. At $t > 150 - 170$ hr, more slow decays of residual and secondary wave modes occur at all altitudes in Figure 4 with decay times τ_0 listed in Table 1 for the steep and sharp wave source activation/deactivation.
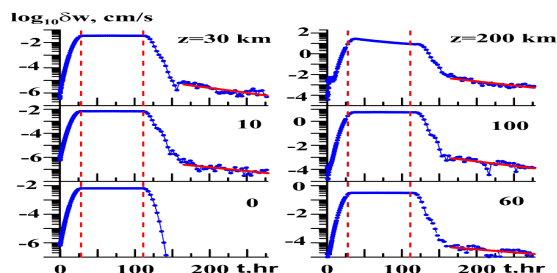
250   **Figure 4.** Same as Figure 2, but for the surface wave source (5) at $c_x = 100$ m/s and $W_0 = 0.1$ mm/s.

Peculiarities of Figure 4 for large W_0 are gradual decreases in AGW amplitudes during the wave source operation between moments t_a and t_d at high altitudes (see the top right panel of Figure 4) in comparison with steady amplitudes in respective panels of Figure 2 for smaller W_0. The reason could be strong generations of wave-induced jet streams by large-amplitude

255 AGWs at high altitudes. Figure 5 shows time variations of horizontal velocity u_0 averaged over a period of the surface wave source (5) with $W_0 = 0.1$ mm/s at different altitudes.
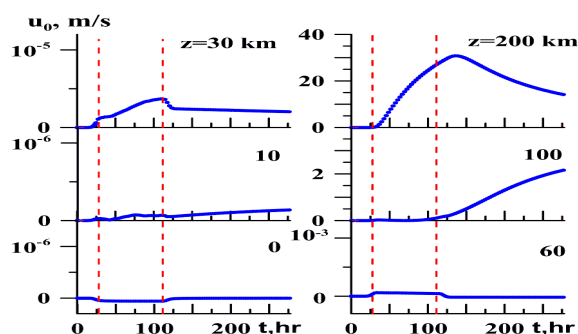
Figure 5. Time variations of the wave induced mean horizontal velocity at different altitudes (marked with numbers) for the
260 steep activations and deactivations of the surface wave source (5) at $c_x = 100$ m/s and $W_0 = 0.1$ mm/s. Dashed lines correspond to $t = t_a$ and $t = t_d$ in (7).

In Figure 5, one can see substantial u_0 rises at altitudes above 100 km during the wave source operation. Rising u_0 decreases the AGW intrinsic frequency and vertical wavelength (e.g., Gossard and Hook, 1975). This may increase wave dissipation due to molecular viscosity and heat conductivity leading to the gradual decrease in AGW amplitude in the right top panel of

265 Figure 4 in the time interval between t_a and t_d. The rate of u_0 weakening after the wave source deactivation decreases slowly in time in the right top panel of Figure 5, so that the wave-induced horizontal winds are still substantial after hundreds wave source periods at high altitudes. An interesting feature is an increase in u_0 at $t > t_d$ in the panel of Figure 5 for $z = 100$ km. This shows that residual and secondary AGWs slowly traveling upwards from below can produce substantial wave accelerations of the mean flow for long time after deactivations of the surface wave sources.

270 Table 2 represents the ratio $\delta w/W_0$ at the moment $t \approx 170$ hr for larger amplitude surface wave sources (5), which may characterize a proportion of residual and secondary waves after disappearing the fast traveling modes of the wave excitation. At steep wave source activations/deactivations with $s_a = s_d \approx 9$ hr, Table 2 demonstrates approximately same $\delta w/W_0$ values below altitude of 100 km and generally smaller values at higher altitudes for $W_0 = 0.1$ mm/s as compared with $W_0 = 0.01$ mm/s, if one considers columns for fixed c_x at different W_0 values. This may be caused by the discussed above transfer of

275 wave energy to wave-induced jets, which can provide also larger reflections and dissipation of wave components with larger amplitudes.

AGW decay times in Table 1 for $W_0 = 0.1$ mm/s at altitudes below 100 km are generally larger for the sharp wave source triggering ($s_a = s_d \approx 0.3$ s) than those for the steep triggering ($s_a = s_d \approx 9$ hr) similar to the case of smaller wave source amplitude discussed in section 3.2. At high altitudes in Table 1 for $W_0 = 0.1$ mm/s, wave decay times for the sharp wave

280 source deactivating become smaller, than those for the steep triggering.

3.4 Spatial structure of AGW fields
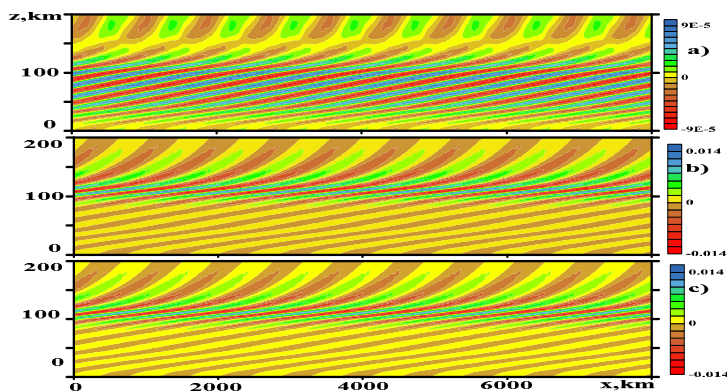
Figure 6. AGW vertical velocity fields at times $t \approx 30$ hr (a), $t \approx 70$ hr (b) and $t \approx 110$ hr (c) for the steep rate of activating/deactivating the wave source (5) with $c_x = 50$ m/s and $W_0 = 0.01$ mm/s.

285 To analyze changes in the spatial structure of simulated AGW fields, Figures 6 and 7 present cross-sections of the field of wave vertical velocity by the XOZ vertical plane at different time moments during activations and deactivations of the surface wave sources (5) with the steep values of $s_a = s_d \approx 9$ hr in (7). Figure 6a shows that after dispersion and dissipation of the initial AGW pulse just after the wave forcing activation time, $t_a \approx 28$ hr, wave fronts become inclined to the horizon. This behavior is characteristic for the main IGW mode with period $\tau \sim 4.7$ hr, which is dominating in the spectrum of the wave

290 source having $c_x = 50$ m/s similar to Figure 1a. In the middle and at the end of quasi-stationary intervals shown in Figures 2 – 4, the inclined wave fronts in Figures 6b and 6c expand to the entire considered XOZ region and wave amplitudes become larger compared to Figure 6a.
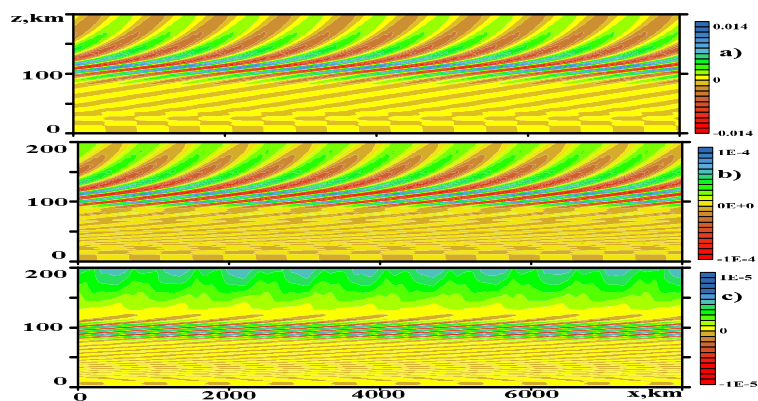
Figure 7. Same as Figure 6, but for time moments after the wave source steep deactivating: $t \approx 140$ hr (a), $t \approx 200$ hr (b) and

295 $t \approx 250$ hr (c).

Cross-sections shown in Figure7 correspond to time moments after the wave source (5) deactivation at $t_d \approx 110$ hr. Figure 7a shows that just after turning off the wave source, the inclined fronts are destroyed, first, in the lower atmosphere. Above altitude 50 km, the wave field structure in Figure 7a is still similar to Figures 6b and 6c. Later, in Figures 7b and 7c, wave

300 amplitudes become smaller, especially at low and high altitudes. Therefore, maximum AGW amplitudes in Figure 7c are located at altitudes 80 – 120 km. This explains the growing wave-induced horizontal velocity at altitude 100 km after the wave source deactivation in the respective panel of Figure 5. At heights below 50 km in Figure 7, directions of wave front inclinations to the horizon are opposite to those in Figure 6. This reveals existence of downward traveling IGW modes in the stratosphere and troposphere after deactivations of the surface wave sources. Such modes could be produces by partial

305 reflections of primary upward traveling IGWs at higher atmospheric levels (see section 4).

Figures 7b and 7c show increasing amounts of small-scale structures, which can be formed by slow shortwave residual wave modes, which appear due to broad wave source spectra in Figure 1 and due to generating secondary waves by nonlinear interactions of primary AGW modes.

4 Discussion

310 The time scale of AGW dissipation in the turbulent atmosphere can be estimated as follows (Gossard and Hook, 1975):

$$\tau_d = \frac{\lambda_z^2}{2\pi K_z},\tag{8}$$

where K_z is the total vertical coefficient of turbulent and molecular viscosity and heat conductivity. For the main primary AGW modes simulated in this study and having $\lambda_z \sim 15 - 30$ km (see section 3.1), $\tau_d \sim 10^3 - 10^5$ hr at altitudes below 100 km. These values are much larger than the AGW decay times τ_0 in Table 1. Therefore, attenuations of primary AGW modes

315 in the middle atmosphere shown in Figures 2 -7 after deactivations of the surface wave forcing cannot be explained by direct turbulent and molecular dissipations.

 AGWs propagating in the atmosphere with vertical gradients of the background fields are subjects to partial reflections. In particular, strong wave reflections occur at altitudes 110 – 150 km, where large vertical gradients of the mean temperature exist (e.g., Yiğit and Medvedev, 2010; Walterscheid and Hickey, 2011; Gavrilov and Kshevetskii, 2018). Partial reflections

320 of wave energy propagating upwards from the wave sources before their deactivations may produce vertically standing waves in the middle atmosphere. Simulations by Gavrilov and Yudin (1987) showed that the standing-wave ratio for IGW amplitudes might reach 0.4 at altitudes below 100 km. After deactivations of wave sources, vertically traveling AGW modes propagate quickly upwards and dissipate at higher atmospheric altitudes. This gives fast decreases in AGW amplitudes at all heights in Figures 2 and 4 just after the wave source deactivations. After disappearing fast traveling modes, residual quasi-

325 standing AGWs produced by partial reflections may form long-lived wave structures in the atmosphere shown in Figures 2 – 7.

 The standing AGWs discussed above are composed of the primary wave modes traveling upwards from the surface wave sources (5) and downward propagating waves reflected at higher atmospheric levels. After the wave source deactivations, the reflected downward waves propagate to the Earth's surface and create wave fronts at low altitudes in Figure 7, which are

330 inclined to the horizon in directions opposite to the fronts of primary AGWs shown in Figure 6. These downward traveling waves are reflected from the ground and propagate upwards back to the middle atmosphere. Kurdyaeva et al. (2018) showed that such AGW reflections from the ground could be equivalent to additional wave forcing at the lower boundary, which is still effective after deactivations of primary surface wave sources. Upward traveling from the ground and reflected again at higher altitudes waves can maintain quasi-standing AGW structures for long time (see Figure 7). As far as wave reflections

335 are partial, portions of wave energy can for long time propagate to higher altitudes and dissipate there. This can explain relatively large AGW decay times τ_0 in the lower and middle atmosphere shown in Figures 2 – 4 and in Table. 1. Even after substantial time from the wave source turning off, AGW structures in Figures 7b and 7c at altitudes above 50 km are still similar to those shown in Figure 6 during active wave forcing.

 Shown in Table 2 ratios $\delta w/W_0$ at $t \approx 170$ km may reflect proportions of the residual and secondary AGW modes in the

340 beginning of quasi-exponential fits in Figures 2 – 4. For the steep wave forcing activations/deactivations, in the right part of Table 2, one can see larger ratios for wave modes with $c_x = 50$ m/s at all altitudes. This corresponds to longer intervals of fast

decreases of AGW amplitudes after deactivations of the wave sources in Figure 4 compared to Figure 2. Considerations of respective right columns of Table 1 reveal larger decay times τ_0 of waves with $c_x = 100$ m/s due to their larger vertical wavelength and smaller dissipation in the middle atmosphere.

345   Comparisons of the right columns in Table 2 with the same c_x and different W_0 show that values of $\delta w/W_0$ for each c_x are approximately equal at altitudes below 60 km and become smaller at higher altitudes for larger amplitude wave sources. This may reflect larger transfers of AGW energy to wave-induced jet streams and to secondary nonlinear modes produced by larger-amplitude waves. Respective right columns of Table 1 show higher decay times τ_0 of larger-amplitude wave noise corresponding to $W_0 = 0.1$ mm/s at altitudes higher 100 km. This noise can be maintained for long time by wave energy

350   fluxes propagating with stronger residual and secondary waves from the middle atmosphere to higher altitudes.

    For the sharp activations/deactivations of the wave sources (5), the left columns of Table 2 show values of $\delta w/W_0$, which are much larger compared to respective right columns for the steep wave forcing triggering. These ratios are less dependent on the speed and amplitude of simulated AGWs and could be connected with wave pulses produced by sharp activations/deactivations of the wave sources (see spectra in Figure 1). AGW decay times for the sharp triggering in

355   respective left columns of Table 1 are also less dependent on wave parameters.

    Substantial amounts of small-scale structures in Figures 7b and 7c shows increased proportions of wave modes, produced due to high-frequency tails of the wave forcing spectra in Figure 1, also due to multiple reflections and nonlinear interactions of these modes. Nonlinear AGW interactions and generations of secondary waves should be stronger at high altitudes due to increased wave amplitudes (Vadas and Liu, 2013; Gavrilov at al., 2015). Then the secondary waves can

360   propagate downwards and make small-scale wave perturbations at all atmospheric altitudes (see Figures 6 and 7). The AGW decay times τ_0 in Table 1 are generally larger for longer AGW modes with $c_x = 100$ m/s. This may be explained by their smaller dissipation due to turbulent and molecular viscosity and heat conductivity in the atmosphere. Due to small coefficients of turbulent dissipation in the stratosphere and mesosphere, maximum AGW decay times in Table 1 exist at altitudes 30 – 100 km. Quasi-standing and secondary AGWs may exist there for several days after deactivations of the wave

365   forcing. Wave energy can slowly penetrate upwards from the stratosphere and mesosphere and maintain a background level of AGW activity at higher altitudes. Figure 7c reveals that after 10 days of simulations, largest amplitudes of the residual wave field exist at altitudes 70 – 110 km. It is enough for creations of wave accelerations, which can act and modify the mean velocity at altitudes near 100 km for the long time after the wave source deactivations (see respective panels of Figure 5).

370   Described above simulations were made for single relatively long AGW spectral components, which experience small dissipation in the stratosphere and mesosphere. Real wave fields in the atmosphere are superpositions of wide range of spectral components generated by a variety of different wave sources. However, after deactivations of wave sources, fast traveling spectral components disperse to higher altitudes and short wave modes are strongly dissipated due to turbulent and molecular viscosity and heat conductivity. Therefore, one may expect that at the final stage of wave disappearing after

375   deactivations of wave forcing, wave fields in the stratosphere and mesosphere should consist of quasi-standing relatively

long spectral components, similar to those considered in the present study. These wave fields may contain substantial proportions of residual and secondary wave modes produced by multiple reflections and nonlinear interactions.

In this paper, we analyzed idealistic cases of long-lived horizontally homogeneous coherent wave sources producing quasi-stationary wave fields in the atmosphere. Such modeling is useful for comparisons of simulated results with standard AGW theories. However, many AGW sources in the atmosphere are local and operate for short time, which is not enough for developments of steady-state wave fields. Further simulations are required for studying wave decay processes after deactivating such local short-lived wave sources in the atmosphere.

5 Conclusion

In this study, the high-resolution numerical model AtmoSym is applied for simulating non-stationary nonlinear AGWs propagating from surface wave sources to higher atmospheric altitudes. After activating the surface wave forcing and fading away initial wave pulses, AGW amplitudes reach a quasi-stationary state. Then the surface wave forcing is deactivated in the numerical model and amplitudes of primary traveling AGW modes quickly decrease at all altitudes due to discontinuation of wave energy generation by the surface wave sources. However, later the standard deviation of the residual and secondary wave perturbations produced by slow components of the wave source spectrum, multiple reflections and nonlinear interactions experiences more slow exponential decreases. The decay time of the residual AGW noise may vary between 20 and 100 hr, having maxima in the stratosphere and mesosphere. Standard deviations of the residual AGWs in the atmosphere are much larger at sharp activations/deactivations of the wave forcing compared to the steep processes. These results show that transient wave sources in the lower atmosphere could create long-lived residual and secondary wave perturbations in the middle atmosphere, which can slowly propagate to higher altitudes and form a background level of wave noise for time intervals of several days after deactivations of wave sources. Such behavior should be taken into account in parameterizations of AGW impacts in numerical models of dynamics and energy of the middle atmosphere.

Data availability. Used high-resolution model of nonlinear AGWs in the atmosphere is available for online simulations (see the reference AtmoSym, 2017). The computer code can be also available under the request from the authors.

Author contributions. SPK participated in the computer code development. AVK prepared background fields for the simulations. NMG made simulations and prepared the initial text of paper, which was edited by all authors.

Competing interests. The authors declare that they have no conflicts of interests.

Acknowledgments. AGW numerical simulations were made in the SPbU Laboratory of ozone layer and upper atmosphere supported by the Ministry of Science and High Education of the Russian Federation (agreement 075-15-2021-583).

Financial support. Calculations of the background fields for simulations were supported by the Russian Science Foundation
410   (grant 20-77-10006).

References

Afraimovich, E. L., Kosogorov, E. A., and Plotnikov, A.V.: Shock–acoustic waves generated during rocket launches and earthquakes, Cosmic Res., 40, 241–254, doi:10.1023/A:1015925020387, 2002.

AtmoSym: Multi-scale atmosphere model from the Earth's surface up to 500 km, http://atmos.kantiana.ru, 2017. (last access
415   on 15.09.2021).

Blanc, E., Farges, T., Le Pichon, A., and Heinrich, P.: Ten year observations of gravity waves from thunderstorms in western Africa, J. Geophys. Res. Atmos., 119 , 6409–6418, doi:10.1002/2013JD020499, 2014.

Dalin, P., Gavrilov, N., Pertsev, N., Perminov, V., A. Pogoreltsev, A., N. Shevchuk, N., Dubietis, A., Völger, P., Zalcik, M., Ling, A., Kulikov, S., Zadorozhny, A., Salakhutdinov, G., and I. Grigoryeva, I.: A case study of long gravity wave crests
420   in noctilucent clouds and their origin in the upper tropospheric jet stream, J. Geophys. Res. Atmos., 121, doi:10.1002/2016JD025422, 2016.

De Angelis, S., McNutt, S. R., and Webley, P. W.: Evidence of atmospheric gravity waves during the 2008 eruption of Okmok volcano from seismic and remote sensing observations, Geophys. Res. Lett., 38(10), doi:10.1029/2011GL047144, 2011.

425   Djuth, F. T., Sulzer, M. P., Gonzales, S. A., Mathews, J. D., Elder, J. H., and Walterscheid, R. L.: A continuum of gravity waves in the Arecibo thermosphere, J. Geophys. Res., 31, L16801, doi:10.1029/2003GL019376, 2004.

Fritts, D. C., and Alexander, M. J.: Gravity wave dynamics and effects in the middle atmosphere, Rev. Geophys., 41(1), 1003, doi:10.1029/2001RG000106, 2003.

Fritts, D. C., Wang, L., Werne, J., Lund, T., and Wan, K.: Gravity wave instability dynamics at high Reynolds numbers. Part
430   II: turbulence evolution, structure, and anisotropy, J. Atmos. Sci., 66, 1149–1171. 2009.

Fritts, D. C., Franke, P. M., Wan, K., Lund, T., and Werne, J.: Computation of clear-air radar backscatter from numerical simulations of turbulence: 2. Backscatter moments throughout the lifecycle of a Kelvin-Helmholtz instability, J. Geophys. Res., 116, D11105, doi:10.1029/2010JD014618, 2011.

Gavrilov, N. V., and Yudin, V. A., Numerical simulation of the propagation of internal gravity waves from nonstationary
435   tropospheric sources, Izvestia, Atmos. and Oceanic Phys., 23(3), 180-186, 1987.

Gavrilov, N. M., and Fukao, S.: A comparison of seasonal variations of gravity wave intensity observed by the MU radar with a theoretical model, J. Atmos. Sci., 56, 3485–3494, 1999.

Gavrilov, N. M., and Kshevetskii, S. P.: Numerical modeling of propagation of breaking nonlinear acoustic-gravity waves from the lower to the upper atmosphere, Adv. Space Res., 51 (7), 1168–1174, doi:10.1016/j.asr.2012.10.023, 2013.

440   Gavrilov, N. M., and Kshevetskii, S. P.: Numerical modeling of the propagation of nonlinear acoustic-gravity waves in the middle and upper atmosphere, Izvestiya, Atmos. Ocean. Phys., 50(1), 66-72, doi:10.1134/S0001433813050046, 2014.

Gavrilov, N. M., and Kshevetskii, S. P.: Verifications of the nonlinear numerical model and polarization relations of atmospheric acoustic-gravity waves, Geosci. Model Dev. Discuss., 7, 7805–7822, 2015.

Gavrilov, N. M., Kshevetskii, S. P., and Koval, A. V.: Propagation of non-stationary acoustic-gravity waves at
445   thermospheric temperatures corresponding to different solar activity, J. Atmos. Solar-Terr. Phys., 172, 100–106, doi: 10.1016/j.jastp.2018.03.021, 2018.

Godin, O.A., Zabotin, N.A., and Bullett, T.W.: Acoustic-gravity waves in the atmosphere generated by infragravity waves in the ocean, Earth Planets Space, 67, 47, doi: 10.1186/s40623-015-0212-4, 2015.

Gossard, E. E., and Hooke, W. H., Waves in the atmosphere, Elsevier Sci. Publ. Co., Amsterdam-Oxford-New York, 1975.

450   Kikoin, I. K.: Tables of Physical Quantities, Atomizdat Press, Moscow, pp. 272–279, 1976.

Kshevetskii, S. P., and Gavrilov, N. M.: Vertical propagation, breaking and effects of nonlinear gravity waves in the atmosphere, J. Atmos. Solar-Terr. Phys., 67(11), 1014–1030, doi: 10.1016/j.jastp.2005.02.013, 2005.

Kurdyaeva, Y., Kshevetskii, S., Gavrilov, N., and Kulichkov, S.: Correct boundary conditions for the high-resolution model of nonlinear acoustic-gravity waves forced by atmospheric pressure variations, Pure Applied Geophys., 175, 1-14, doi:
455   10.1007/s00024-018-1906-x, 2018.

Liu, X., Xu, J., Gao, H., and Chen, G.: Kelvin-Helmholtz billows and their effects on mean state during gravity wave propagation, Ann. Geophys., 27, 2789-2798, 2009.

Medvedev, A. S., and Gavrilov, N. M.: The nonlinear mechanism of gravity wave generation by meteorological motions in the atmosphere, J. Atmos. Terr. Phys., 57, 1221–1231, 1995.

460   Medvedev, A. S., and Yĭgit, E.: Gravity waves in planetary atmospheres: Their effects and parameterization in global circulation models, Atmosphere, 10, 531, doi:10.3390/atmos10090531, 2019.

Mellado, J. P., Bretherton, C. S., Stevens, B., and Wyant, M. C.: DNS and LES for simulating stratocumulus: Better together, J. Adv. Modeling Earth Syst., 10, 1421– 1438, doi: 10.1029/2018MS001312, 2018.

Meng, X., Vergados, P., Komjathy, A., and Verkhoglyadova, O.: Upper atmospheric responses to surface disturbances: An
465   observational perspective, Radio Sci., 54(11), 1076-1098, doi: 10.1029/2019RS006858, 2019.

Park, J., Lühr, H., Lee, C., Kim, Y. H., Jee, G., and Kim J.-H.: A climatology of medium-scale gravity wave activity in the midlatitude/low-latitude daytime upper thermosphere as observed by CHAMP, J. Geophys. Res. Space Phys., 119, doi:10.1002/2013JA019705, 2014.

Picone, J. M., Hedin, A. E., Drob, D. P., and Aikin, A.C.: NRLMSISE-00 empirical model of the atmosphere: Statistical
470   comparisons and scientific issues, J. Geophys. Res., 107(A12), 1468, doi:10.1029/2002JA009430, 2002.

Pielke, Sr. R., Cotton, W., Walko, R., Tremback, C., Lyons, W., Grasso, L., Nicholls, M., Moran, M., Wesley, D., Lee, T., Copeland, J.: A comprehensive meteorological modeling system-RAMS, Meteorol. Atmos. Phys., 49, 69-91, doi: 10.1007/BF01025401, 1992.

Rapoport, Y. G., Gotynyan, O. E., Ivchenko, V.M., Kozak, L.V., and Parrot, M.: Effect of acoustic-gravity wave of the lithospheric origin on the ionospheric F region before earthquakes, Physics and Chemistry of the Earth, , Elsevier, 2004, 29 (4-9), 607-616, doi:10.1016/j.pce.2003.10.006, 2004.

Townsend, A. A.: Excitation of internal waves by a turbulent boundary layer, J. Fluid. Mech., 22, 241–252, 1965.

Townsend, A. A.: Internal waves produced by a convective layer, J. Fluid. Mech., 24, 307–319, 1966.

Vadas, S. L., and Fritts D. C.: Influence of solar variability on gravity wave structure and dissipation in the thermosphere from tropospheric convection, J. Geophys. Res., 111, A10S12, doi:10.1029/2005JA011510, 2006.

Vadas, S. L., and Liu, H.-L.: Numerical modeling of the large-scale neutral and plasma responses to the body forces created by the dissipation of gravity waves from 6 h of deep convection in Brazil, J. Geophys. Res. Space Physics, 118, 2593–2617, doi: 10.1002/jgra.50249, 2013.

Walterscheid, R. L., and Hickey, M. P.: Group velocity and energy flux in the thermosphere: Limits on the validity of group velocity in a viscous atmosphere, J. Geophys. Res. Atmospheres, 116(D12), doi: 10.1029/2010JD014987, 2011.

WRF: The weather research and forecasting model, https://www.mmm.ucar.edu/wrf-user-support-contributor-information, 2019. (last excess 15 September, 2021).

Wu, J. F., Xue, X. H., Hoffmann, L., Dou, X. K., Li, H. M., and Chen, T. D.: A case study of typhoon-induced gravity waves and the orographic impacts related to Typhoon Mindulle (2004) over Taiwan, J. Geophys. Res., 120(18), 9193-9207, doi:10.1002/2015JD023517, 2015.

Yiğit, E., and Medvedev, A.S.: Internal gravity waves in the thermosphere during low and high solar activity: Simulation study, J. Geophys. Res., 115, A00G02, doi: 10.1029/2009JA015106, 2010.

Yiğit, E., and Medvedev A.S.: Internal wave coupling processes in Earth's atmosphere, Adv. Space Res., doi: 10.1016/j.asr.2014.11.020, 2014.

Yu, Y., Wang, W., Hickey M. P., Ionospheric signatures of gravity waves produced by the 2004 Sumatra and 2011 Tohoku tsunamis: A modeling study, J. Geophys. Res. Space Phys., 122(1), 1146-1162, doi: 10.1002/2016JA023116, 2017.